IEEE Access
Multidisciplinary | Rapid Review | Open Access Journal

Received June 8, 2021, accepted August 4, 2021, date of publication August 23, 2021, date of current version August 31, 2021.

Digital Object Identifier 10.1109/ACCESS.2021.3106710

Transducer Arrays Over A^{2}B Networks in Industrial and Automotive Applications: Clock Propagation Measurements

N. ROCCHI, A. TOSCANI, G. CHIORBOLI, D. PINARDI, M. BINELLI, AND ANGELO FARINA

Department of Engineering and Architecture, University of Parma, 43125 Parma, Italy

Corresponding author: N. Rocchi (nicholas.rocchi@unipr.it)

ABSTRACT Advanced automotive applications like Active Noise Cancellation (ANC) and Individual Listening Zones (ILZ) require a high number of transducers (i.e., microphones, accelerometers, and loudspeakers) usually arranged as arrays. Transducer arrays are widely employed in several applications besides automotive field, such as teleconferencing systems, industrial and civil monitoring of noise and vibrations. Automotive Audio Bus (A^{2}B) is an audio transport protocol that solves the latest requirements of automotive and industrial fields. A^{2}B allows transporting up to 32 channels in a multi-node daisy chain network and guarantees synchronization and low deterministic latency. This paper aims to develop a clock propagation model of an A^{2}B network composed by transducer arrays. This model will be useful to evaluate the impact of the bus on the array performance. Firstly, a theoretical description of the A^{2}B protocol and jitter analysis is provided. It follows a description of the jitter measures carried out on the clocks distributed along the A^{2}B network. Lastly, latency introduced by nodes of the network is investigated.

INDEX TERMS Data communication, industrial communication, jitter, latency, microphone array, transducer array.

I. INTRODUCTION

In the last decades, due to the need of designing smarter and more efficient vehicles, the number of electronic components and connections in cars has massively increased. Traditionally, control signals and transducers data were transported over CAN bus, which combines all these signals in a reduced number of cables [1], [2].

Recently, we have seen an increasing interest in the innovation of car audio systems thanks to new technologies like Active Noise Cancellation (ANC) [3]–[5], Individual Listening Zones (ILZ) [6] and innovative Noise, Vibration and Harshness (NVH) analysis techniques. These technologies require a high number of microphones, accelerometers, and loudspeakers mounted in the car [3], [7]. An analog wiring of these devices would be too expensive and heavy, whilst today's digital transmission protocols are not suited for the real-time transmission of a high number of audio channels. Two protocols that are currently used in infotainment systems are MOST and AVB [8]–[10]. Despite their flexibility and performance, management components of these protocol stacks are expensive. In addition, they do not guarantee phase alignment in signals and a low deterministic latency, which is mandatory for ANC [11] and control applications [12].

Automotive Audio Bus (A^{2}B) is a protocol developed by Analog Devices that solves the previously mentioned problems. A^{2}B allows connecting multiple nodes (one master and up to ten slaves) in a daisy-chain configuration. This bus can transport up to 32 audio channels in each direction over an Unshielded Twisted Pair (UTP) cable, which allows reducing costs and weight compared to analog or Ethernet cables. Moreover, A^{2}B is designed to guarantee a very low and deterministic latency. Slave nodes in the bus are synchronized by the master node, which is fed with a low jitter clock. Each node will then recover the master clock from the packets transmitted over the bus.

As hinted in [13], A^{2}B can be employed in several fields besides automotive. For instance, vibration data acquisition systems and industrial monitoring systems (e.g., vibrational analysis of beverage filler machines, conveyor belts or industrial robots) employ a high number of transducers, whose output signals are acquired synchronously and in real-time.

The associate editor coordinating the review of this manuscript and approving it for publication was Theofanis P. Raptis.

Micro Electronic Mechanical Systems (MEMS) transducers are an optimal solution because they feature a digital output, ensuring a full-digital system. Instead, if analog transducers are employed (e.g., piezoelectric), Analog-to-Digital converters can be embedded in A²B nodes. In this way, any pre-existing transducer network can be acquired by an A²B system.

One of the most widespread technology employed in industrial systems is based on ethernet networks [14], [15], which require expensive devices to manage the protocol [16]. A²B can be used to synchronously collect a high number of sensor signals, keeping the overall system cost low by using cheap cables (single UTP instead of ethernet cable) and dedicated low-cost transceivers. A²B features and low implementation cost make it suitable for consumer electronics too. For example, teleconferencing or immersive audio reproduction systems employ an increasing number of microphones and loudspeakers arranged in arrays for the implementation of beamforming. For the best performance, these systems require a very low and constant latency as well as phase aligned signals.

Since an A²B network has a daisy-chain topology, the clock is propagated along the nodes cascade, degrading its quality in terms of jitter and latency as the number of the node increases. This may lead to an overall worsening of the system performance, especially for those applications where synchronous sampling is required. In this paper, the clock propagation of an A²B network is investigated with particular focus on jitter and latency. Section II provides a brief explanation of the main features of the A²B protocol. In sections III and IV, jitter modelling and its effects are discussed. Section V describes the measures carried out and shows the obtained results. Finally, in section VI the developed clock propagation model is presented, and section VII concludes the paper.

II. A²B NETWORK

An A²B network is a multi-node protocol with a single master and up to ten slaves connected in a daisy-chain topology. It allows transporting digital audio and control signals over distance. The maximum cable length between the master node and the last slave is 40 m, whilst the maximum distance between two nodes is 15 m [17].

A²B has a total bandwidth of 50 Mbit/s, which allows transporting up to 32 downstream and upstream audio channels with a sample rate of 44.1 kHz or 48 kHz and sample width of 16 bits, 24 bits, or 32 bits. *Downstream* is the communication flow from the master node to the last slave node, whilst *upstream* is the communication flow from the last slave node to the master node. In Fig. 1, an example of A²B network is shown. As can be seen, audio data is transferred locally in I²S/TDM format, which is typically used for inter-IC communication of digital audio, or in PDM format which is often employed by MEMS microphones.

In addition to audio channels, I²C commands and GPIO signals can be transmitted to other nodes. This feature

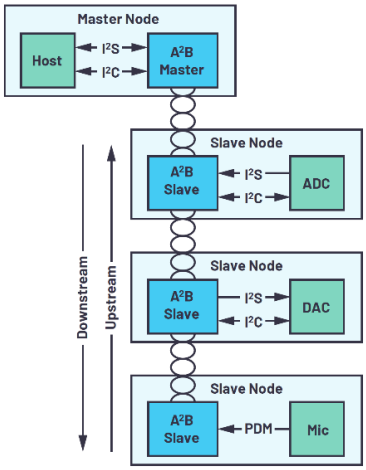

FIGURE 1. Example of an A²B network composed by a master node and three slave nodes. The host processor connected to the master node configures the network and streams audio. Each slave can be connected to ADCs, DACs, DSPs, or PDM microphones (picture from [13]).

can be particularly useful if devices connected to slave nodes need to be configured at power-on. Usually, this task is carried out by a microcontroller embedded in the slave node, but the A²B host processor connected to the master node can configure all the devices in the slave nodes.

A²B is not a plug and play protocol. The network must be initialized by the host processor connected to the master node. This task is divided in two phases: *discovery* and *initialization*. In the discovery phase the host processor checks for the presence of the slave nodes, whilst in the initialization it configures slave nodes and their peripherals. Once the network is configured, the audio stream starts. The communication starts with the downstream phase from the master node, which sends to the first slave a packet, called *superframe* (Fig. 2).

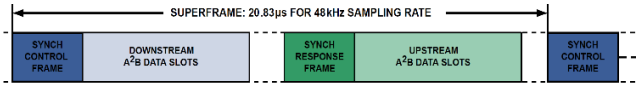

FIGURE 2. Structure of the A²B superframe. The blue half includes the downstream header (SCF) and payload. The green half includes the upstream header (SRF) and payload. Each slave node of the network recovers its sampling frequency from the superframe (picture from [17]).

When a slave receives the superframe, it can use or consume the *audio slots* and then it passes the packet to the next node. An audio slot is a sample of an audio channel. The last slave of the chain, after accessing the audio slots, sends the superframe back to the previous slave adding its audio slots. This phase is called upstream, and it ends when the master receives again the superframe. Downstream and upstream are performed within one sampling period, namely 20.83 μs at a sampling frequency of 48 kHz.

The superframe starts with a Synch Control Frame (SCF). The SCF contains a *preamble*, which is used by the slave nodes to synchronize their clocks and it also embeds GPIO over distance and I²C data. After the SCF, it follows the

payload, which contains the downstream audio slots. Each audio slot is up to 32 bits wide and there can be up to 32 audio slots. After the downstream payload, a new header, called Synch Response Frame (SRF), and an upstream payload are transmitted by the last slave to the upstream slaves. As for the downstream, each node receiving the superframe adds or consumes audio slots and then it passes the packet to the next node, until it reaches the master.

It shall be pointed out that all the nodes are sampled synchronously in the same A²B superframe. To achieve this result, data received on the I²S/TDM port of an A²B transceiver are transmitted over the A²B bus in the next superframe, whilst data received from the A²B bus are transmitted to the I²S/TDM port in the next superframe. Thus, data exchanged between two nodes have a latency of two superframes. Moreover, the internal delays introduced by the A²B transceivers and the delay due to the cable length must be considered to calculate the correct value of the latency. However, these last components of delay can be compensated by setting in each A²B transceiver an offset value of the frame clock. This allows a perfect phase alignment of the signals, with a resolution of about 20 ns, that is a period of the bus clock. The phase alignment is achieved by means of the synchronization of all the nodes. The host generates I²S/TDM signals, which are fed to that master. The latter transmits the superframes in the A²B network at the frame clock signal rate. As previously said, the SCF contains a preamble used by the slaves' PLL to recover the clock signal. Since all the slave nodes recover the clock from the superframe transmission rate, it is of main importance for the frame clock fed to the master node to be a low jitter clock.

III. JITTER MODELING AND DECOMPOSITION

Total jitter (TJ), which is defined as the deviation of transition edges from their ideal position to the actual one in time domain, can be mainly decomposed into unbounded random jitter (RJ) and bounded deterministic jitter (DJ), depending on the underlying sources producing them [18]–[21]. RJ typically follows an unbounded Gaussian distribution, and it is quantified using the standard deviation of this distribution. However, jitter distribution is not often Gaussian, due to the contribution of the DJ, which can be expressed in terms of subcomponents of various origin, namely the periodic jitter (PJ), the bounded uncorrelated jitter (BUJ) and the data-dependent jitter (DDJ). PJ is usually related to ground bounce and power supply switching noise that couples to data or clock signal lines [22]. BUJ is due to crosstalk between aggressor and victim channels and DDJ is caused by asymmetry in rise time and fall time, or by bandwidth limitation of the channel [23].

The amount of total jitter, with its distribution and spectrum, can be directly measured in the time domain. However, simply specifying jitter through peak-to-peak or RMS values, which is always possible, can be inadequate, because of the different impact of RJ and DJ on a link performance. Several approaches have been proposed for jitter decomposition in the last decades, based on tail-fitting algorithms or FFT analysis.

A. JITTER DECOMPOSITION BASED ON CDF

Since RJ and DJ are independent, the probability density function of TJ is the convolution of the RJ and DJ pdf. The effect of the RJ is to smear with its tail the tailless deterministic jitter distribution that, in the Dual-Dirac model, is usually approximated by two delta functions in $x = \pm\mu$ [19]. Starting from a Gaussian distributed RJ with mean μ and standard deviation σ, the cumulative function of the RJ is given by

$$CDF\,(x) = \frac{1}{2}\left(1 + erf\left(\frac{x-\mu}{\sigma\sqrt{2}}\right)\right) \tag{1}$$

where erf is the error function. From the experimental Cumulated Histogram of the total jitter, CH(x), we define the Q scale as

$$Q = \sqrt{2}erf^{-1}\,(2CH\,(x) - 1) \tag{2}$$

where erf^{-1} is the inverse error function.

In the Q scale, a pure Gaussian distribution is a straight line with slope σ^{-1} and intercept μ (μ_L and μ_R for the left and the right tail of the general TJ distribution, respectively). Therefore, σ is estimated by means of a least squares linear fitting of Q for very large values of x. The quantity $\mu_R - \mu_L$ accounts for the effect of the DJ components and is often referred to as Dual-Dirac DJ ($DJ_{\delta\delta}$). However, even if the DJ follows a distribution formed by two Dirac-delta functions, the Q scale generally underestimates the peak-to-peak DJ and overestimates the RJ [19]. To better account for the contribution of the DJ pdf, a normalized Q scale is described in [24]. Recently, [25] demonstrated that the jitter distribution tails approach a Gaussian pdf multiplied by a term that is inversely proportional to the TJ and proposed an enhanced method of decomposition.

B. JITTER DECOMPOSITION IN TIME AND FREQUENCY DOMAINS

Real-time oscilloscopes can display single shot jitter trend and perform FFT analysis to determine frequency content. The jitter spectrum can be obtained by applying averaging techniques and the narrow-band peaks in the spectrum can be interpreted as PJ or DDJ. Conversely, the noise floor in the average spectrum points out the power of RJ.

IV. CLOCK JITTER EFFECTS

Clock jitter results in an equivalent additive noise in data converters. For a sinusoidal input signal $x\,(t) = A\sin\,(2\pi f_i t)$ and a sampling clock affected by the timing jitter t_j, the equivalent noise induced by jitter is approximatively given by $x_{nj}\,(t) = A2\pi f_i t_j \cos\,(2\pi f_i t)$. Assuming, for the sake of simplicity, only RJ with standard deviation σ_j, the noise power related to the jitter is

$$N_j = \left(A^2\big/2\right)\left(2\pi f_i \sigma_j\right)^2 \tag{3}$$

This contribution must be compared with the quantization noise power, that is of the order of $q^2/12$, where q represents the least significant bit of the converter. It is apparent that N_j is of some interest mainly for high-frequency or high-resolution Analog-to-Digital converters, stimulated by high-level signals. For instance, for a 14-bit ADC operating at 100 MHz, the jitter should be below 100 *fs* to worsen the SNR less than 3 dB. A timing jitter $\sigma_j = 200$ ps at $f_i = 10$ kHz reduces the effective resolution to 16 bits [26].

Similar considerations can be made for Digital-to-Analog Converters (DAC) followed by analog low-pass filters, when only the in-band noise power due to jitter is considered [19].

V. EXPERIMENTAL RESULTS

Investigations on jitter and latency of an A^{2}B network are justified by its clock recovery mechanism and its daisy chain architecture. In addition, no in-depth public documentation is provided on this topic.

With the aim of measuring the impact of jitter on the clock recover performance and the latency introduced by the nodes, an A^{2}B network composed by a master and ten slaves was built (Fig. 3).

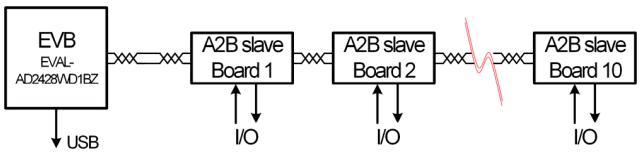

FIGURE 3. Architecture of the A^{2}B network used during the tests.

The A^{2}B master employed is an Analog Devices evaluation board (EVAL-AD2428WD1BZ). In addition to the A^{2}B chip, it is also equipped with a SigmaDSP (the audio host) and an USB interface. The internal PLL of the SigmaDSP generates the clock for the entire network, whilst the USB interface allows the A^{2}B network to be configured using a PC. All of the slave nodes are equal in hardware, and they are equipped with two MEMS microphones. Although A^{2}B is designed for automotive and industrial applications, for the sake of simplicity measures were carried out in a laboratory environment.

The entire network can be configured using the graphic development software SigmaStudio (Fig. 4). The three blocks on the left are the target processor (the device that configures the network), the audio host (the device that feeds the clock to the network and manages I/O audio) and the A^{2}B master node (in dark grey). The remaining blocks are the slave nodes (in light grey) and their peripherals (in light blue), namely the devices that can input or output audio. Measures and data acquisitions were carried out using a Teledyne LeCroy HDO6000 high-definition oscilloscope (12 bits) featuring 350 MHz bandwidth and 2.5 GSa/s of sampling rate. Since the vertical scale and the time range of the HDO6000 were set, respectively, to 500 mV/div and to 10 ms

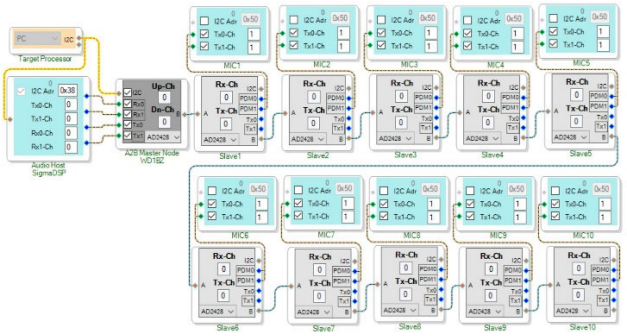

FIGURE 4. SigmaStudio project of the A^{2}B network used during the tests.

or less, the jitter measurement floor of the instrument was estimated to be smaller than 5 ps.

A. FRAME CLOCK JITTER MEASUREMENTS

There are several ways to measure jitter. The most meaningful for a clock recovery system are cycle-to-cycle jitter and Time Interval Error (TIE).

The cycle-to-cycle jitter measures how much the clock period changes between any two adjacent cycles and it shows the instantaneous dynamics that a clock-recovery PLL might be subjected to [27].

Thus, to evaluate the short-term effect of the jitter on the 48 kHz sampling frequency (Fig. 2), the cycle-to-cycle jitter was measured for each node of the network, starting from the master to the last slave.

The values of cycle-to-cycle jitter were measured by the oscilloscope and plotted in a histogram. Fig. 5 shows cycle-to-cycle jitter measures for every A^{2}B node and for two different cable lengths between the master and the first slave.

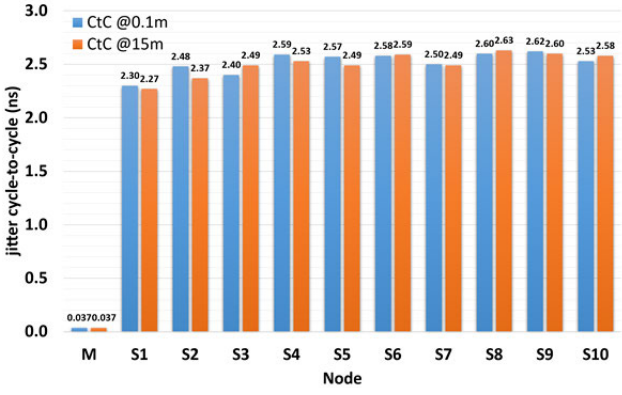

FIGURE 5. Cycle-to-cycle jitter of the sampling frequency, for different nodes and for different cable lengths between the master and the first slave.

Thus, the slave nodes were close one to each other (few centimetres), whilst it was varied the distance between the master node and the first slave. This configuration emulates applications that relies on microphone or speaker arrays.

As it can be seen, the cycle-to-cycle jitter is lower for the master node because it is equipped with an on-board

crystal oscillator, whilst slave nodes recover the clock using a local PLL (phase-locked loop) locked on the superframe transmission frequency.

As expected, the cycle-to-cycle jitter shows negligible dependence on both the length of the cable and the number of slave nodes.

For a more detailed jitter characterization, ''long-term effects'' were investigated. The TIE shows the cumulative effect that even a small amount of period jitter can have over time, by measuring how far each active edge of the clock varies from its ideal position [27].

Firstly, 1 MSamples of TIE were acquired for ensuring a statistical uncertainty well below the 1% [19]. The oscilloscope LeCroy HDO6000 has the capability to directly measure the TIE. An acquisition example is shown in Fig. 6.

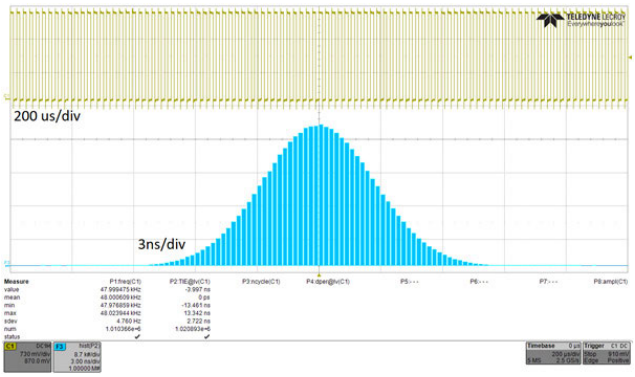

FIGURE 6. Oscilloscope acquisition of sampling clock (upper trace) and TIE histogram (lower trace). The histogram has 1 MSamples of TIE.

The upper trace is the sampling frequency of an A^{2}B slave node, whilst the lower trace is the TIE histogram elaborated by the oscilloscope. With this setup, 1 MSamples of TIE were acquired for the first, fifth and tenth slave node. A post-processing analysis of the acquired data was carried out to decompose RJ and DJ.

The TIE histograms of all the slave nodes can be well fitted with a Gaussian function (Fig. 7), obtaining an adjusted R-squared always better than 0.9999, that points out the preponderance of RJ.

Since the CDFs in Q-scale (Fig. 8) showed the same slope for the left and right tails, the normalized Q-scale transform was not used.

Table 1 shows the extracted values of RJ and DJ components for some slaves. Since the tail fitting method assumes that the right (left) peak of the dual-Dirac DJ distribution does not contribute to the left tail (right, respectively), an accurate decomposition of the two contributions is possible only when the two Dirac pulses are sufficiently separated. The extracted DJ contribution, however, was of one order of magnitude smaller than RJ component and therefore the accuracy of the method is questionable.

Therefore, jitter spectra obtained by averaging 32 TIE spectra highlights a narrow-band peaks ranging from 170 ps to 140 ps at 12 kHz and confirms the reported TJ in the band

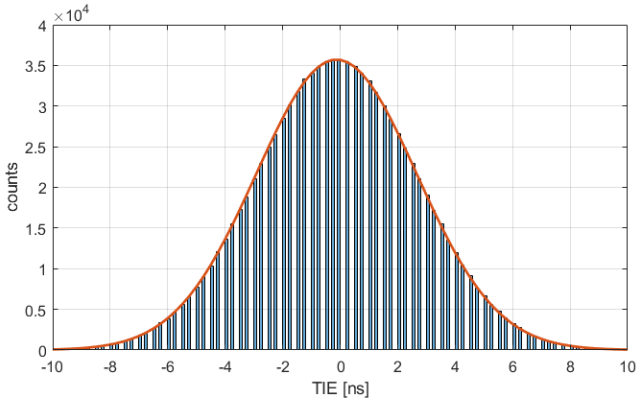

FIGURE 7. The TIE histogram of the 10th slave, with the fitting Gaussian function.

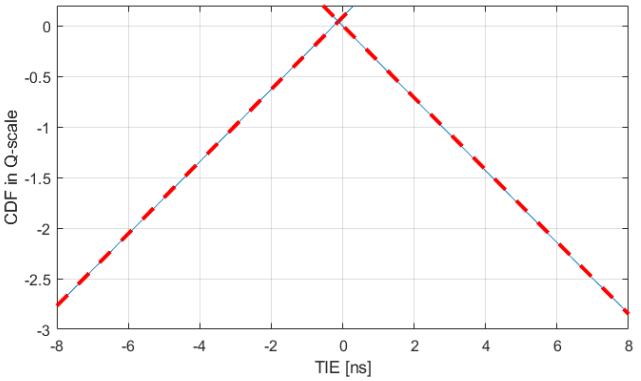

FIGURE 8. The CDF in Q scale for TIE of the 10th slave, with the fitting straight lines, from left and from sides.

TABLE 1. RJ and DJ from CDF in Q-scale.

Slave	RJ	DJ
1	1.6 ns	100 ps
5	2.2 ns	170 ps
10	2.8 ns	250 ps

above 100 Hz. The jitter component at 12 kHz was previously reported also in [28].

Afterword, TIE measures were carried out for all the slave nodes with the same setup used for the previous measurement.

Fig. 9 shows the TIE for different nodes and for different cable lengths between the master and the first slave.

As for the cycle-to-cycle jitter, the TIE of the master node clock is lower than in slave nodes, and the effects of the cable length are negligible.

The cycle-to-cycle jitter does not depend on the node number, whilst the TIE increases as the number of the slave node increases. The reason is that each node recovers the clock from the superframe received on one port and it retransmits it to the other port, causing the jitter to accumulate along the bus.

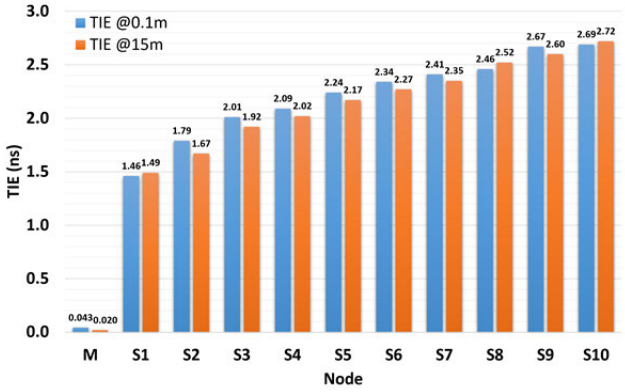

FIGURE 9. TIE of the sampling frequency, for different nodes and for different cable lengths between the master and the first slave.

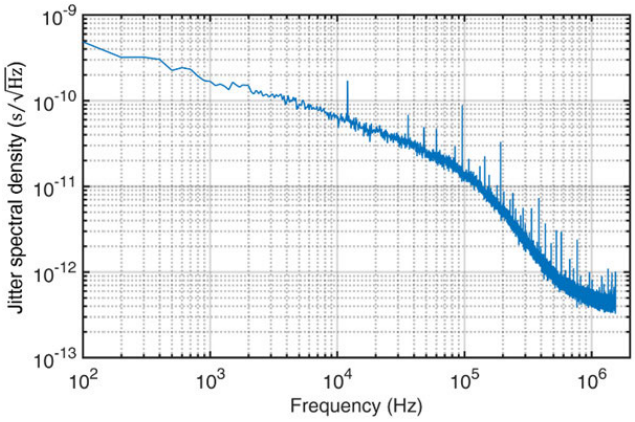

FIGURE 10. Bit clock jitter spectral density of the 1st slave.

B. BIT CLOCK JITTER MEASUREMENTS

Some transducers (i.e., PDM microphones) require bit clock instead of frame clock because they oversample the audio signal. For this reason, this subsection analyses TIE values and TIE spectrum of the bit clock in a few nodes of the A^{2}B network.

To this aim, 5 MSamples TIE histograms of the bit clock were acquired at the 1st, 5th and 9th slave nodes. Once again, the histograms were fitted with a Gaussian function, obtaining an adjusted R-squared always better than 0.9999, which points out the preponderance of RJ. The CFD in Q-scale was again used for a first attempt to decompose RJ and DJ and the obtained estimates were similar to those reported for the frame clock. These estimates were compared with those provided by the TIE spectra that were evaluated by averaging 34 spectra obtained by acquiring the TIE for 10 ms, i.e., approximatively, 30720 $\times$ 34 samples. There are several narrowband peaks at the frequencies equal to $(k \times 48) \pm 12$ kHz, as shown in Fig. 10. The bit clock spectra corresponds with the frame clock spectra in the frequency range from 100 Hz to 24 kHz. The peak levels, due to DJ, slightly decrease by moving from the first to the last slave, probably for a beneficial dithering effect of the increasing RJ. The results are summarized in Table 2.

TABLE 2. RJ and DJ of bit clock.

	CDF in Q-scale		Averaged spectra	
Slave	RJ	DJ	RJ	DJ
1	1.6 ns	103 ps	1.6 ns	225 ps
5	2.3 ns	246 ps	2.3 ns	223 ps
9	2.9 ns	254 ps	2.9 ns	195 ps

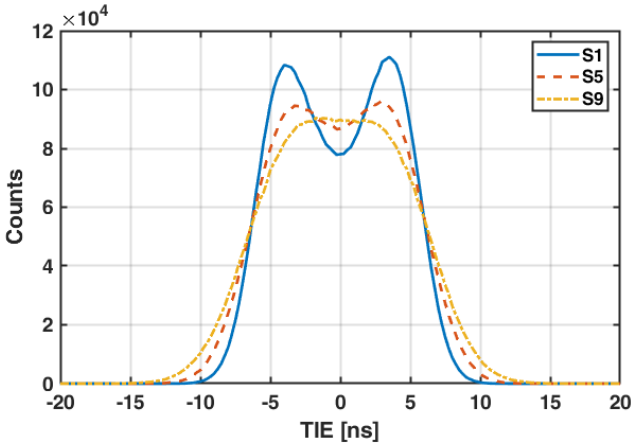

FIGURE 11. TIE histograms of 1st, 5th, and 9th A^{2}B slave node. Spread spectrum in low depth mode was enabled.

In addition, the A^{2}B transceiver features a two depth levels spread spectrum for reducing the radiated power per unit bandwidth [29]. This feature affects the bit clock but not the frame clock. Thus, the effect of the two depth modes (low and high) on the bit clock jitter were investigated for the 1st, 5th, and 9th slave node.

When the low depth spread spectrum is enabled, the TIE jitter on the bit clock increases and the histogram in Fig. 11 is clearly the result of the convolution of RJ and DJ. Fig. 11 reports the histograms for different slaves (1st, 5th, and 9th). It shows that for the slaves closer to the master, the components due to spread spectrum modulation are more noticeable.

In the previously discussed conditions, the normalized CDF in Q-scale was conveniently used to decompose RJ and DJ contribution. Fig. 12 reports the data obtained for the same case of the 1st slave.

The jitter spectral density of the 1st slave changes as shown in Fig. 13, with an apparent increase of the narrowband components above 144 kHz, and particularly at 336 kHz (7.3 ns).

Fig. 14 compares two oscilloscope acquisitions of the histograms of the bit clock TIE jitter, one with high depth and the other with low depth spread spectrum for the 5th slave node. As it can be seen, the behaviour is similar for low and high depth modes, but in high depth mode the DJ is greater with respect to the low mode. In addition, the TIE standard deviation, as expected, is increased with high depth spread spectrum.

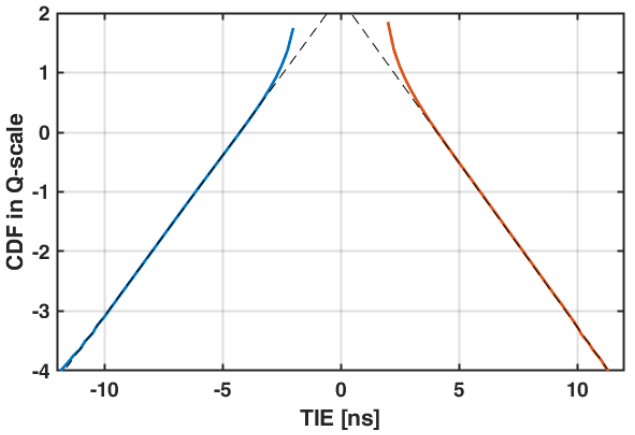

FIGURE 12. The CDF in Q scale for TIE of the 1st slave, with the fitting straight lines, from left and from sides.

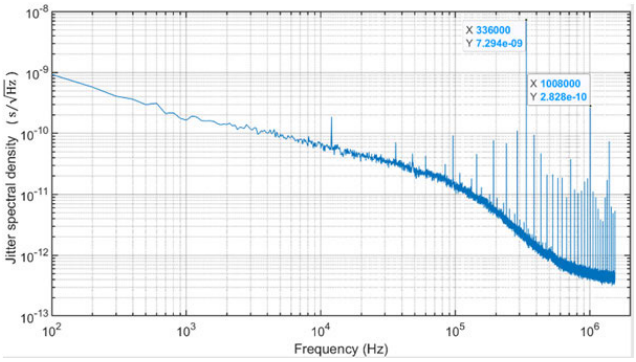

FIGURE 13. Bit clock jitter spectral density of the 1st slave, with high depth spread spectrum enabled.

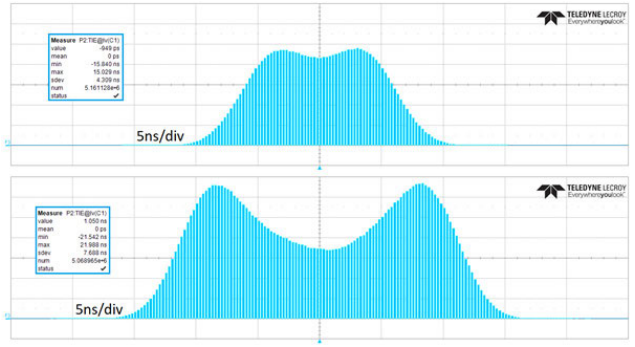

FIGURE 14. TIE histograms of the 5th slave node (spread spectrum low depth mode, top trace; spread spectrum high depth mode, bottom trace). Scale of the x-axis: 5 ns/div.

Finally, in Table 3, the results of deconvolution of RJ and DJ contribution for both cases of spread spectrum in low depth and high depth mode are summarized.

C. LATENCY MEASUREMENTS

For any analog/digital interface system and especially for microphone or speaker arrays, the sampling clock delay between each device is crucial. Thus, the delay propagations of the clock in the entire A^{2}B network were investigated.

TABLE 3. RJ and DJ obtained from normalized CDF in Q-scale.

	Low depth spread spectrum mode		High depth spread spectrum mode	
Slave	RJ	DJ	RJ	DJ
1	1.86 ns	8.16 ns	2.02 ns	17.6 ns
5	2.44 ns	8.35 ns	2.56 ns	17.6 ns
9	3.11 ns	7.87 ns	3.17 ns	17.4 ns

In Fig. 15, the audio frame clock edges are shown for the master node (top trace) and for different slave nodes (1st, 5th, and 10th top to bottom). The jitter effects are clearly visible thanks to the digital persistence of the oscilloscope, but they are negligible with respect to the delay.

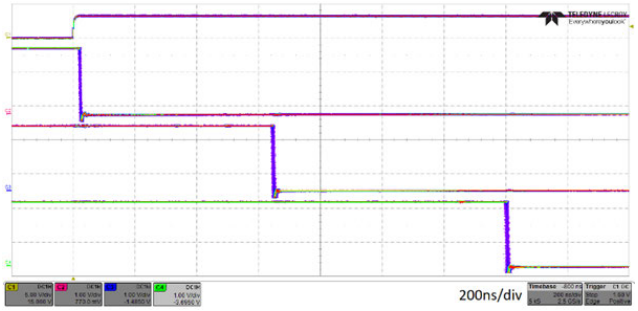

FIGURE 15. Clock edges of the master and slave nodes (master node, 1st, 5th and 10th top to bottom).

In Fig. 16, it is shown the delay introduced by each slave node measured with respect to the first slave node for two different cable lengths between the nodes. As it can be seen, the experimental points fit a straight line. This means that each node adds a constant delay. Slightly different delay values are obtained for the two cable lengths, pointing out that the propagation delay in the cables is not negligible.

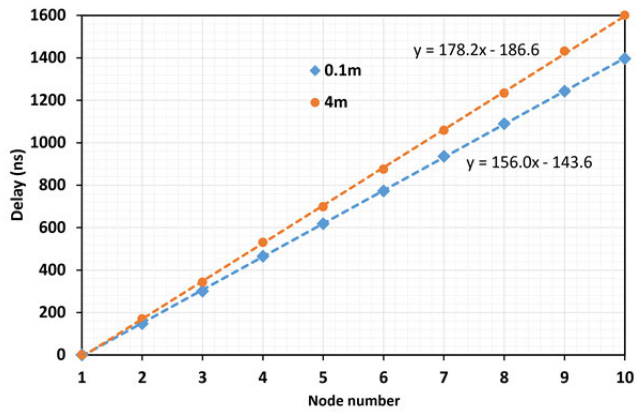

FIGURE 16. Delay introduced by each slave node, measured with respect to the first slave node for two different cable lengths between the nodes.

To prove that the delay introduced by each node is deterministic and constant, further measures were performed. The skew between two clock edges of two consecutive slave nodes

was measured to obtain a histogram (Fig. 17). The skew was measured between two positive edges of the frame clock, at 50 % of signal level. 150 kSamples were acquired to obtain the histogram.

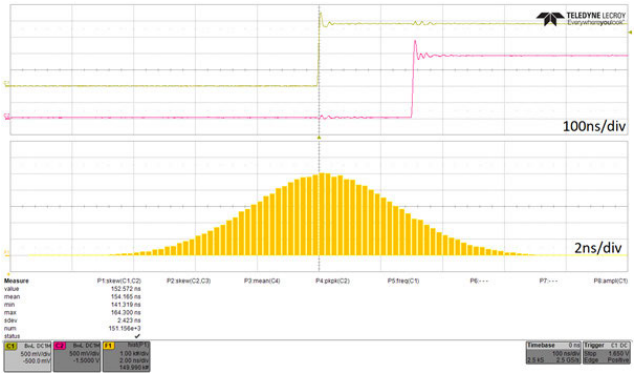

FIGURE 17. Skew measure. Positive edges of the frame clock of the 8th slave (top grid, yellow trace) and of the 9th slave (top grid, red trace). Skew histogram (bottom grid).

The results of these measures are shown in Fig. 18. This figure shows the mean value of the delay introduced by each node with its respective standard deviation. As it can be seen, the propagation delay is nearly constant and the mean value over all the slaves is 154.14 ns. This value is compliant to the datasheet of the A^{2}B transceiver [30].

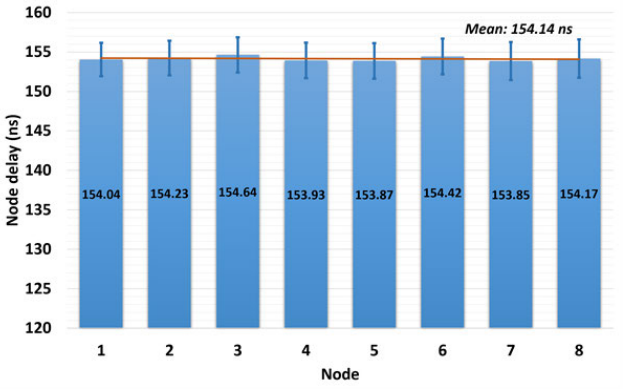

FIGURE 18. Delay introduced by each slave node. The value of each bar is the mean value of the histogram. The standard deviation is shown over each bar.

Each A^{2}B slave can compensate for its propagation delay thanks to a feature of the protocol. In fact, an A^{2}B slave chip can adjust the start of the audio frame with a resolution of about 20.35 ns, corresponding to the period of the bus clock (1/49.152 MHz at a sampling frequency of 48 kHz), by writing the appropriate value into a register of the transceiver. The result of this operation can be seen in Fig. 19, where the propagation delay between the 1st and the 9th slave has been compensated.

Finally, further measures were carried out to evaluate the propagation delay introduced by the cables. The delay

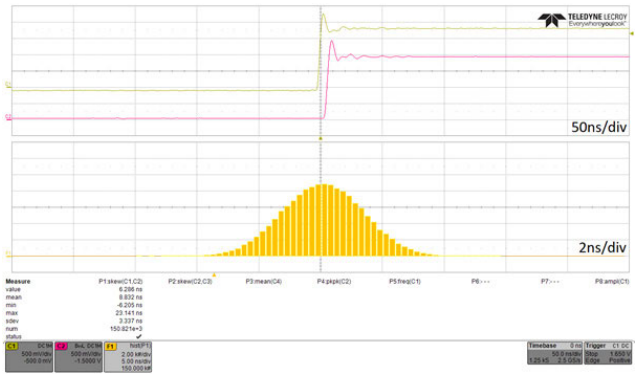

FIGURE 19. Oscilloscope capture of the skew measured between the 1st and 9th slaves (top grid), after propagation delay compensation. Related histogram (bottom grid).

between clock edges of the first and second slave nodes for different cable lengths is plotted in Fig. 20. Experimental points fit a straight line with equation $y{=}mx{+}q$, where q it the delay of a single node and m is the inverse of the propagation speed of the cable ($2.7{\cdot}10^8$ m/s).

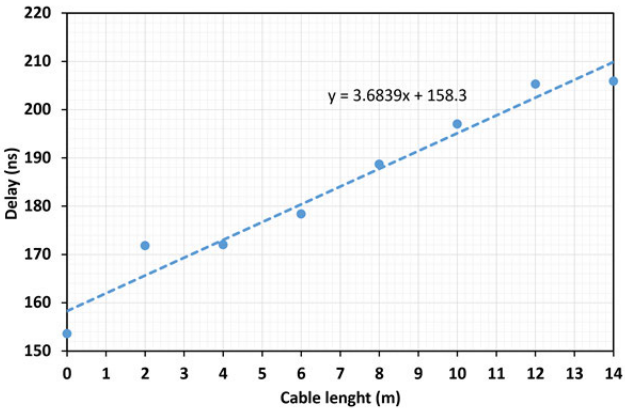

FIGURE 20. Delay between clock edges of the first and the second slave node for different cable lengths.

VI. CLOCK PROPAGATION MODEL

At the conclusion of the previous clock measurements, a fully comprehensive model can be summarized. Assuming the master node clock as a reference, the first slave shows a random TIE distribution, fully described using the standard deviation. The other nodes show the same random distribution, but with a slight increase of the standard deviation value (see Fig. 9).

Since only slave nodes input or output signals, the zero-time reference is taken on the first slave. Each of the following slaves introduce a deterministic mean delay of 154.14 ns (see Fig. 18). As previously discussed, this delay can be compensated with a resolution of about 20 ns.

As an application example, the proposed model is useful specifically for designing transducer arrays, such as microphone arrays. Numerical methods are widely employed for

predicting the spatial performance of such systems in terms of directivity as a function of frequency, which consists in computing the polar patterns of the virtual microphones obtained through beamforming. By introducing the proposed clock model in the numerical simulations post-processing, the effects of the delay and jitter are considered. It will result in a deviation of the polar patterns with respect to the theoretical ones, that is, a reduction of directivity.

VII. CONCLUSION

In this paper, after a brief description of the A²B protocol and jitter modelling and decomposition, a full set of measures carried out on an A²B network prototype are presented. The network was composed by a master node and ten slaves, with input/output capability.

Firstly, jitter and latency measures were carried out, then, a critical analysis of the obtained results led to the development of a clock propagation model.

As result from the measures, the jitter presents a predominant random component (RJ), whilst the deterministic component (DJ) can be neglected. RJ follows an unbounded Gaussian distribution, and it is quantified using the standard deviation of this distribution.

The latency, conversely, is deterministic and can be compensated with a resolution of about 20 ns, using an A²B protocol feature. The measures show that the mean of this latency is 154.14 ns for each slave node.

In addition, A²B offers the possibility of reducing electromagnetic emissions per unit bandwidth by enabling spread spectrum on high frequency clock signals. This feature affects the jitter behaviour, by slightly increasing the RJ component and introducing a no longer negligible DJ component.

The proposed clock propagation model can be used to evaluate more accurately the beamforming performance of transducer arrays in numerical simulations, which are typically purely geometrical. It allows considering the effects of delay and jitter, which may cause a reduction of the directivity. Authors are currently studying beamforming with A²B microphone arrays, and a future work will present the effects introduced by the clock propagation investigated in this paper.

REFERENCES

[1] J. Huang, M. Zhao, Y. Zhou, and C.-C. Xing, "In-vehicle networking: Protocols, challenges, and solutions," *IEEE Netw.*, vol. 33, no. 1, pp. 92–98, Jan./Feb. 2019, doi: 10.1109/MNET.2018.1700448.

[2] J. Wang, J. Liu, and N. Kato, "Networking and communications in autonomous driving: A survey," *IEEE Commun. Surveys Tuts.*, vol. 21, no. 2, pp. 1243–1274, 2nd Quart., 2019, doi: 10.1109/COMST.2018.2888904.

[3] J. Boehm *et al.*, "A distributed audio system for automotive applications," *J. Audio Eng. Soc., Eng. Brief*, vol. 450, pp. 1–6, May 2018.

[4] C.-Y. Chang, A. Siswanto, C.-Y. Ho, T.-K. Yeh, Y.-R. Chen, and S. M. Kuo, "Listening in a noisy environment: Integration of active noise control in audio products," *IEEE Consum. Electron. Mag.*, vol. 5, no. 4, pp. 34–43, Oct. 2016, doi: 10.1109/MCE.2016.2590159.

[5] V. Patel, J. Cheer, and S. Fontana, "Design and implementation of an active noise control headphone with directional hear-through capability," *IEEE Trans. Consum. Electron.*, vol. 66, no. 1, pp. 32–40, Feb. 2020, doi: 10.1109/TCE.2019.2956634.

[6] G. Pepe, L. Gabrielli, S. Squartini, L. Cattani, and C. Tripodi, "Deep learning for individual listening zone," in *Proc. IEEE 22nd Int. Workshop Multimedia Signal Process. (MMSP)*, Sep. 2020, pp. 1–6, doi: 10.1109/MMSP48831.2020.9287161.

[7] S. M. Kuo, H. Chuang, and P. P. Mallela, "Integrated automotive signal processing and audio system," *IEEE Trans. Consum. Electron.*, vol. 39, no. 3, pp. 522–532, Jun. 1993, doi: 10.1109/30.234630.

[8] S. Poferl, M. Becht, and P. De Pauw, "150 Mbit/s MOST, the next generation automotive infotainment system," in *Proc. 12th Int. Conf. Transparent Opt. Netw.*, Jun. 2010, pp. 1–2, doi: 10.1109/icton.2010.5549160.

[9] A. Sabry, A. Omar, M. Hammad, and N. Abdelbaki, "AVB/TSN protocols in automotive networking," in *Proc. 15th Int. Conf. Comput. Eng. Syst. (ICCES)*, Dec. 2020, pp. 1–7, doi: 10.1109/ICCES51560.2020.9334667.

[10] L. Lo Bello, R. Mariani, S. Mubeen, and S. Saponara, "Recent advances and trends in on-board embedded and networked automotive systems," *IEEE Trans. Ind. Informat.*, vol. 15, no. 2, pp. 1038–1051, Feb. 2019, doi: 10.1109/TII.2018.2879544.

[11] K. Waurin, "Innovative digital bus architecture reduces audio system costs," Analog Devices, Norwood, MA, USA, Tech. Rep., 2018. [Online]. Available: https://www.analog.com/media/en/technical-documentation/tech-articles/Innovative-Digital-Bus-Architecture-Reduces-Audio-System-Costs.pdf

[12] T. P. Raptis, A. Passarella, and M. Conti, "Data management in industry 4.0: State of the art and open challenges," *IEEE Access*, vol. 7, pp. 97052–97093, 2019, doi: 10.1109/ACCESS.2019.2929296.

[13] J. Triggs, "The A to Z of A²B Applications," *Analog Dialogue*, vol. 54, no. 3, pp. 1–4, Sep. 2020.

[14] C. Gang, Y. Dong, and C. Rensheng, "Developing trend of industrial fieldbus control system," in *Proc. 8th Int. Conf. Electron. Meas. Instrum.*, Aug. 2007, pp. 1-765–1-768, doi: 10.1109/ICEMI.2007.4350563.

[15] B. Xi, Y. Fang, M. Chen, and J. Liu, "Use of Ethernet for industrial control networks," in *Proc. 1st IEEE Conf. Ind. Electron. Appl.*, May 2006, pp. 1–4, doi: 10.1109/ICIEA.2006.257288.

[16] S. Bao, H. Yan, Q. Chi, Z. Pang, and Y. Sun, "FPGA-based reconfigurable data acquisition system for industrial sensors," *IEEE Trans. Ind. Informat.*, vol. 13, no. 4, pp. 1503–1512, Aug. 2017, doi: 10.1109/TII.2016.2641462.

[17] *AD2420(W)/6(W)/7(W)/8(W)/9(W) Automotive Audio Bus A²B Transceiver Technical Reference*, Analog Devices, Norwood, MA, USA, 2019.

[18] W. Maichen, *Digital Timing Measurements: From Scopes and Probes to Timing and Jitter*. New York, NY, USA: Springer, 2006.

[19] N. da Dalt and A. Sheikholeslami, *Understanding Jitter and Phase Noise*. Cambridge, U.K.: Cambridge Univ. Press, 2018.

[20] *Information Technology—Fibre Channel—Part 117: Methodologies for Jitter and Signal Quality (MJSQ)*, Standard ISO/IEC TR 14165-117:2007(R2018), 2018.

[21] C. Travis and P. Lesso, "Specifying the jitter performance of audio components," in *Proc. AES 117th Conv.*, 2004, pp. 1–15. [Online]. Available: https://www.aes.org/e-lib/online/browse.cfm?elib=12950

[22] J. N. Tripathi, V. K. Sharma, and H. Shrimali, "A review on power supply induced jitter," *IEEE Trans. Compon., Packag., Manuf. Technol.*, vol. 9, no. 3, pp. 511–524, Mar. 2019, doi: 10.1109/TCPMT.2018.2872608.

[23] J. Buckwalter, B. Analui, and A. Hajimiri, "Predicting data-dependent jitter," *IEEE Trans. Circuits Syst. II, Exp. Briefs*, vol. 51, no. 9, pp. 453–457, Sep. 2004, doi: 10.1109/TCSII.2004.834537.

[24] M. Miller and M. Schnecker, "A comparison of methods for estimating total jitter concerning precision, accuracy and robustness," in *Proc. DesignCon*, 2007, pp. 1–24.

[25] G. Soliman, "Improved jitter distribution tail-fitting algorithm for decomposition of random and deterministic jitter," *IEEE Trans. Electromagn. Compat.*, vol. 62, no. 5, pp. 1852–1858, Oct. 2020, doi: 10.1109/TEMC.2019.2947222.

[26] B. A. Blesser, "Digitization of audio: A comprehensive examination of theory, implementation, and current practice," *J. Audio Eng. Soc.*, vol. 26, no. 10, pp. 739–771, 2012.

[27] *Understanding and Characterizing Timing Jitter*, Tektronix, Beaverton, OR, USA, 2017, pp. 1–20.

[28] *Technote 008 A²B I²S Clock Jitter*, Clockworks, Shrewsbury, U.K., 2020, pp. 1–31.

[29] J.-W. Lee, H.-J. Kim, and C. Yoo, "Spread spectrum clock generation for reduced electro-magnetic interference in consumer electronics devices," *IEEE Trans. Consum. Electron.*, vol. 56, no. 2, pp. 844–847, May 2010, doi: 10.1109/TCE.2010.5506010.

[30] *AD2420(W)-AD2426(W)-AD2427(W)-AD2428(W)-AD2429(W) Datasheet*, Analog Devices, Norwood, MA, USA, 2020.

N. ROCCHI received the B.S. and M.S. degrees *(cum laude)* in electronic engineering from the University of Parma, Italy, in 2017 and 2019, respectively, where he is currently pursuing the Ph.D. degree in information technology.

His research interests include multichannel audio distribution, acquisition systems, and audio amplifiers.

A. TOSCANI received the M.S. degree *(cum laude)* in electronic engineering and the Ph.D. degree in information technology from the University of Parma, Italy, in 2004 and 2008, respectively.

Since 2004, he has been working with the Department of Information Engineering (now, the Department of Engineering and Architecture), University of Parma. He is currently a Research Fellow, mainly focused on power electronics, high-performance electric drives, diagnostic techniques for industrial electric systems, and power converter for audio application. He is the author of two patents.

G. CHIORBOLI received the M.S. degree *(cum laude)* in electronic engineering from the University of Bologna, Bologna, Italy, in 1987. He is currently an Associate Professor of electronic measurements with the University of Parma, Parma, Italy. His current research interests include electronic instruments and sensors, analog-to-digital and digital-to-analog modeling and testing, and electrical characterization of semiconductor devices.

D. PINARDI received the M.S. degree *(cum laude)* in mechanical engineering from the University of Parma, Italy, in July 2016, with a thesis on loudspeaker modeling, and the Ph.D. degree in industrial engineering, in March 2020, with a thesis on the design of microphone, hydrophone, and camera arrays for spatial audio recording.

Since 2016, he has been a Research Assistant of Prof. Angelo Farina, mainly specialized in spatial audio. His research interests include design of transducer arrays, acoustics simulations and 3D auralization, applied to automotive field, and underwater acoustics.

M. BINELLI received the B.S. and M.S. degrees in electronic engineering from the University of Parma, Italy, in 2003 and 2006, respectively, and the Ph.D. degree from the University of Parma, in 2010, with a thesis on analysis and equalization techniques in automotive acoustics.

Since 2010, he has been working as a Research Assistant with University of Parma. His research interests include equalization, psychoacoustics, active noise control, microphones and loudspeakers arrays, virtual reality, and spatial audio.

ANGELO FARINA received the M.S. degree in civil engineering from the University of Bologna, Italy, in December 1982, with a thesis on the acoustics and vibrations inside a tractor cab, and the Ph.D. degree in technical physics from the University of Bologna, in 1987, with a thesis on experimental assessment of concert hall acoustics.

He has been a full-time Researcher with the University of Bologna, since November 1986, and the University of Parma, since March 1992. In November 1998, he became an Associate Professor with the University of Parma, where he has been a Full Professor of environmental applied physics, since May 2005. He was the Chair of applied acoustics and technical physics with the University of Parma. During his academic career, he worked in several fields of applied acoustics, including noise and vibration, concert hall acoustics, simulation software, and advanced measurement systems. In the last ten years, he focused mostly on applications involving massive microphone and loudspeaker arrays. He is the author of more than 300 scientific articles and three widely employed software packages, such as Ramsete, Aurora Plugins, and DISIA.

Dr. Farina was awarded with the AES Fellowship for his pioneering work on electroacoustic measurements based on exponential sine sweeps.